Asian Journal of Chemistry; Vol. 38, No. 2 (2026), 352-358
ASIAN JOURNAL OF CHEMISTRY
https://doi.org/10.14233/ajchem.2026.34973

A Dual-Strategic Approach to Synthesize Fe_2O_3 Nanoparticles with Study on their Structural, Optical and Antibacterial Properties

SARASWATI GHADAI[1], SUCHISMITA ACHARYA[1,*], MAMALISA SAHOO[2], MONALI PRIYADARSINI MISHRA[2], S.K. BISWAL[1] and S.N. SARANGI[3]

[1]School of Applied Sciences, Centurion University of Technology and Management, Jatni, Bhubaneswar-752050, India
[2]School of Paramedics and Allied Health Sciences, Centurion University of Technology and Management, Jatni, Bhubaneswar-752050, India
[3]Institute of Physics, Sachivalaya Marg, Bhubaneswar-751005, India

*Corresponding author: E-mail: suchismita.acharya@cutm.ac.in

Received: 27 September 2025 *Accepted*: 20 December 2025 *Published online*: 31 January 2026 AJC-22253

In this study, iron(III) oxide (Fe_2O_3) nanoparticles were synthesized using two approaches namely a conventional chemical co-precipitation method and a green synthesis route utilizing *Azadirachta indica* leaf extract, which simultaneously functions as a reducing and stabilizing agent. Following synthesis, the nanoparticles underwent characterization to assess their optical behaviour along with structural and morphological features. Through XRD characterization, Fe_2O_3 was identified in its rhombohedral crystalline configuration, with average particle sizes measured as 42 nm for co-precipitation-derived samples and 35 nm for those synthesized *via* the green route. Scanning electron microscopy (SEM) revealed size variations between the two synthesis routes, with the green method producing relatively smaller and more uniformly dispersed nanoparticles. UV-Vis absorption spectra indicated the characteristic optical transitions with slight band gap variations, attributed to particle size and surface modifications by phytochemicals present in the neem extract. Fourier-transform infrared spectroscopy revealed characteristic Fe–O bond vibrations together with biomolecular groups in Fe_2O_3 nanoparticles produced *via* the neem-assisted route. Antimicrobial testing performed using the agar well diffusion method against *Staphylococcus aureus* and *Escherichia coli* showed that the green-synthesized particles achieved greater inhibition zones. This enhancement is associated with their nanoscale size, enlarged surface-to-volume ratio and the functional bioactive molecules originating from neem extract. Overall, the study underscores the potential of green synthesis for designing effective and biocompatible antibacterial nanomaterials.

Keywords: Fe_2O_3 nanoparticles, Green synthesis, *Azadirachta indica*, Antibacterial activity.

INTRODUCTION

Transition metal oxide (TMO) nanomaterials constitute a highly versatile class of functional materials due to their distinctive physico-chemical, structural, electronic and surface properties [1,2]. Their tunable band gaps, high surface-to-volume ratios, chemical stability and catalytic activity have enabled widespread applications in catalysis, energy storage, sensing, optoelectronics, magnetic devices and biomedicine [1-4]. Among TMOs, iron(III) oxide (Fe_2O_3) has attracted considerable interest owing to its low-cost, chemical stability, environmental compatibility and biocompatibility [5-7]. Fe_2O_3 exists in several polymorphic forms, including hematite (α), maghemite (γ) and the β-phase, with α-Fe_2O_3 being the most thermodynamically stable under ambient conditions and therefore the most extensively studied [6,7]. The narrow band gap of α-Fe_2O_3 (~2.2 eV) allows efficient visible-light absorption, making it suitable for photocatalytic and photoelectrochemical applications [8]. Its antiferromagnetic behaviour, with a Néel temperature of approximately 956 K, further supports potential use in magnetic and spintronic devices [9]. In addition, the low toxicity and strong chemical stability of α-Fe_2O_3 favour its application in biomedical fields such as drug delivery, magnetic resonance imaging, biosensing and antimicrobial coatings [10-13].

At the nanoscale, α-Fe_2O_3 nanoparticles exhibit enhanced reactivity owing to increased surface area and a higher density of active sites, resulting in improved catalytic efficiency and biological interactions [10-12,14,15]. These nanoparticles can generate reactive oxygen species (ROS), leading to oxidative stress, membrane disruption and interference with essential cellular processes in microorganisms, thereby inhibiting bact-

erial growth. Such antibacterial properties are valuable for applications in medical devices, antimicrobial coatings, and water purification systems [14,16-18]. Many studies have also reported effective antibacterial activity against various microbial strains, with mechanisms involving ROS-induced damage, membrane destabilization and Fe–protein interactions that ultimately lead to bacterial cell death [16,19,20].

Given these attributes, the development of scalable and environmentally benign synthesis strategies is essential. Green synthesis approaches offer advantages such as reduced environmental impact and improved nanoparticle dispersibility and stability in biological media, thereby enhancing antimicrobial performance through favourable surface chemistry [14,16-18]. These considerations emphasize the need for optimized eco-friendly synthesis routes that enable precise control over nanoparticle size, surface characteristics and functional activity.

A range of synthetic approaches, both physical and chemical, are employed to obtain Fe_2O_3 nanoparticles, with common examples being sol-gel, hydrothermal and solvothermal techniques, microemulsion, thermal decomposition, co-precipitation and chemical vapour deposition [21,22]. Among the various synthesis strategies, the co-precipitation method remains one of the most widely adopted approaches owing to its simplicity, cost-effectiveness, scalability and ability to produce nanoparticles with uniform physico-chemical properties [21-23]. In recent years, increasing emphasis has been placed on green synthesis routes as sustainable alternatives to conventional chemical methods [23-25]. These eco-friendly approaches utilize plant extracts, microorganisms or natural polymers as multifunctional reducing, capping and stabilizing agents, thereby enabling environmentally benign nanoparticle production [23-26].

Plant-mediated synthesis, in particular, has attracted significant interest due to the rich diversity of bioactive phytochemicals such as alkaloids, polyphenols, flavonoids, terpenoids and proteins, which play a crucial role in both the reduction of metal precursors and the stabilization of the resulting nanoparticles [25,27]. This strategy eliminates the need for hazardous chemicals and high-temperature processing, while simultaneously yielding stable, biocompatible and functionally enhanced nanoparticles suitable for biomedical and environmental applications. In this context, the present study systematically compares iron oxide (Fe_2O_3) nanoparticles synthesized through a conventional co-precipitation method and a green synthesis route employing neem (*Azadirachta indica*) leaf extract. The investigation encompasses a comprehensive assessment of the structural and optical properties of the synthesized nanoparticles, along with an evaluation of their antibacterial efficacy against *Staphylococcus aureus* (Gram-positive) and *Escherichia coli* (Gram-negative) bacterial strains. Through this comparative approach, the study aims to bridge the conventional and eco-friendly synthesis strategies for Fe_2O_3 nanoparticles by elucidating the influence of the synthesis route on their physico-chemical characteristics and antibacterial performance.

EXPERIMENTAL

Synthesis of Fe_2O_3 nanoparticles: Iron(III) oxide (Fe_2O_3) nanoparticles were synthesized using two distinct approaches *viz*. a conventional chemical co-precipitation method (CFO) and a green synthesis route employing *Azadirachta indica* (neem) leaf extract (GFO). In both procedures, $FeCl_3 \cdot 6H_2O$ was used as the iron precursor, NH_4OH served as the precipitating agent and distilled water acted as the reaction medium.

Conventional co-precipitation method (CFO): In the co-precipitation process, 0.50 g of $FeCl_3 \cdot 6H_2O$ was dissolved in 20 mL of distilled water and magnetically stirred for 5 min at a controlled temperature of 40-50 ºC to ensure complete dissolution. Subsequently, NH_4OH was added dropwise under vigorous stirring until the pH reached 10-11, facilitating the complete precipitation of $Fe(OH)_3$. The resulting suspension was continuously stirred for 3 h under ambient conditions to promote particle growth and homogeneity. The precipitate was then aged and repeatedly washed with double distilled water followed by ethanol to remove residual impurities. The washed product was oven-dried at 80 ºC for 12 h and subsequently calcined at 400-500 ºC for 3 h, yielding crystalline Fe_2O_3 nanoparticles.

Green synthesis using neem leaf extract (GFO): For the green synthesis route, fresh neem leaves were thoroughly washed with distilled water, air-dried and finely ground. Approximately 10-20 g of the resulting paste was boiled in 100 mL of distilled water for 15-20 min to extract bioactive phytochemicals. The extract was filtered and stored at 4 ºC for subsequent use. In the nanoparticle synthesis step, 0.5 g of $FeCl_3 \cdot 6H_2O$ was dissolved in 20 mL of distilled water and mixed with 20 mL of the prepared neem leaf extract under continuous stirring followed by the addition of NH_4OH dropwise to adjust the pH to 10-11 while maintain the reaction mixture at 60-80 ºC for 2 h. The appearance of a reddish-brown precipitate indicated the formation of Fe_2O_3 nanoparticles. The precipitate was collected, thoroughly washed with double distilled water and acetone and dried at 80 ºC for 12 h. Final calcination was carried out at 300 ºC for 3 h to obtain bio-functionalized Fe_2O_3 nanoparticles.

Characterization: The crystalline structure and phase purity of Fe_2O_3 were studied using an X-ray diffractometer (Bruker D8 Advance) equipped with Cu*K*α radiation (λ = 1.5406 Å) in the 2θ range of 20º-80º. The morphology and surface features of the synthesized nanoparticles were examined using SEM (Zeiss Ultra 55 at 5 kV). UV-Vis absorption spectra were acquired using a Shimadzu spectrophotometer over the 200-800 nm range. FTIR analysis was performed with a Perkin-Elmer instrument between 4000-500 cm^{-1} to identify the functional groups.

Antibacterial activity: The antibacterial activity of the synthesized Fe_2O_3 nanoparticles was evaluated against *S. aureus* (Gram-positive) and *E. coli* (Gram-negative) using the agar well diffusion method. Nutrient agar plates were prepared and uniformly inoculated with freshly grown bacterial cultures using sterile cotton swabs to obtain confluent lawns. Sterile wells/discs were then placed on the agar surface and loaded with predetermined volumes of nanoparticle suspensions under aseptic conditions. The inoculated plates were incubated at 37 ºC for 24 h. After incubation, antibacterial activity was assessed by measuring the diameters of the zones of inhibition formed around the wells/discs.

RESULTS AND DISCUSSION

XRD studies: Both CFO (co-precipitation route) and GFO (green route) Fe_2O_3 samples exhibited sharp and intense diffraction peaks, demonstrating their well-defined crystalline nature as illustrated in Fig. 1. The observed reflections at ~24.26º (012), 33.37º (104), 35.76º (110), 41.10º (113), 49.55º (024), 54.25º (116), 57.62º (018), 62.74º (214), 64.12º (300), 71.91º (1010) and 75.58º (220) are in good agreement with the standard JCPDS data for hematite (α-Fe_2O_3), confirming the formation of a pure crystalline phase without secondary impurities [17]. These peaks correspond well to the standard diffraction pattern of α-Fe_2O_3 (hematite) with a rhombohedral crystal structure, indexed to the JCPDS card no. 33-0664, confirming the successful formation of the hematite phase in both samples [15-17,20]. The lack of secondary or spurious peaks demonstrates that the nanoparticles obtained are phase-pure and uncontaminated. The diffraction peaks of the green-synthesized Fe_2O_3 (GFO) appear slightly broader compared to those of the chemically synthesized Fe_2O_3 (CFO), which indicates the formation of smaller crystallite sizes in the green synthesis route. The average crystallite size (D) was calculated using the Debye-Scherrer's equation:

$$D = \frac{0.9\lambda}{\beta \cos\theta}$$

where D stands for crystallite size; α is the X-ray wavelength (1.5406 Å, Cu*K*α); β corresponds to the full-width at half maximum of the diffraction peak (radians); and θ is the Bragg angle. The evaluation revealed comparatively larger crystallites in CFO (42 nm), while GFO (35 nm) displayed smaller crystallite dimensions, which can be linked to the capping and stabilizing effects of phytochemicals present in neem leaf during nanoparticle formation [28]. The enhanced peak intensity in the CFO sample indicates slightly better crystallinity compared to GFO sample, whereas the reduced intensity and peak broadening in GFO sample suggest the presence of surface biofunctionalization imparted by phytochemicals during green synthesis [29].

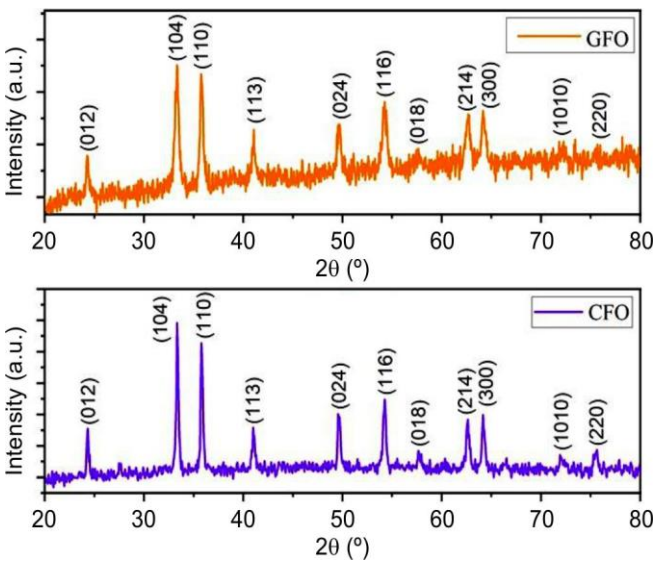

Fig. 1. X-ray diffraction spectra of Fe_2O_3 nanoparticles

The phytochemicals may adhere to the particle surface, causing lattice strain or defects, which further influences the crystallite size and broadening of peaks [28,29]. The estimated structural parameters, including lattice constants, unit cell volume and microstrain, were found to be in close agreement with standard α-Fe_2O_3 data, supporting the presence of a stable rhombohedral hematite structure [15,16,20]. The smaller crystallite size of the GFO nanoparticles is advantageous for enhanced surface reactivity and antibacterial performance.

FESEM studies: FESEM micrographs reveal distinct morphology and size evolution in Fe_2O_3 obtained by the two synthesis routes. For the co-precipitation sample (Fig. 2a-b), the powder consists of densely packed, faceted plate-/flake-like crystallites stacked into compact aggregates. Individual plates show well-defined edges and smooth terraces, with lateral dimensions typically in the sub-micron to ~1-2 μm range and thicknesses of a few hundred nanometers. Numerous finer nanoparticles are seen decorating the plate surfaces and interstices, suggesting secondary nucleation on preformed facets during growth. The high packing density and sharp faceting indicate relatively rapid growth along preferred crystallographic directions during calcination, yielding a more compact microstructure with lower open porosity.

In contrast, the green-synthesized sample using *A. indica* extract (Fig. 2c-d) exhibits a much more open, fluffy morphology composed of loosely connected nanoaggregates. Higher magnification images show nearly spherical to sub-rounded primary particles forming a porous network. The primary particle size is predominantly in the ~30-90 nm range, with occasional clusters up to ~120 nm due to agglomeration. The lack of pronounced faceting and the narrower particle size suggest that phytochemicals in the neem extract act as capping/stabilizing agents, increasing the nucleation rate while inhibiting anisotropic growth and limiting particle coarsening during calcination. The resulting meso-/nano-porous architecture provides a higher accessible surface area relative to the co-precipitated counterpart. The morphological contrast between the two routes aligns with the XRD observations as the smaller primary particles in the green route are consistent with broader diffraction peaks (smaller crystallite size), whereas the sharper faceted plates in co-precipitated sample correspond to higher crystallinity and larger coherent domains. Some degree of particle clustering is observed in both samples, which is expected for iron oxide owing to magnetic dipole-dipole interactions and capillary forces during drying. However, clustering is less compact in the green sample because the organic residues during synthesis help maintain inter-particle spacing prior to calcination.

The optical absorption spectra of the synthesized Fe_2O_3 nanoparticles obtained *via* green synthesis (GFO) and co-precipitation (CFO) routes are shown in Fig. 3. The presence of intense absorption bands in the UV and visible ranges indicates the typical optical behaviour associated with α-Fe_2O_3 nanoparticles in both samples [30-32]. The CFO sample exhibits a pronounced absorption edge near ~410 nm, while the GFO sample shows a red-shifted edge at around ~430 nm. This shift in the GFO spectrum suggests a reduction in the optical band-gap energy, which is often attributed to surface modifications, or the presence of phytochemical capping agents from

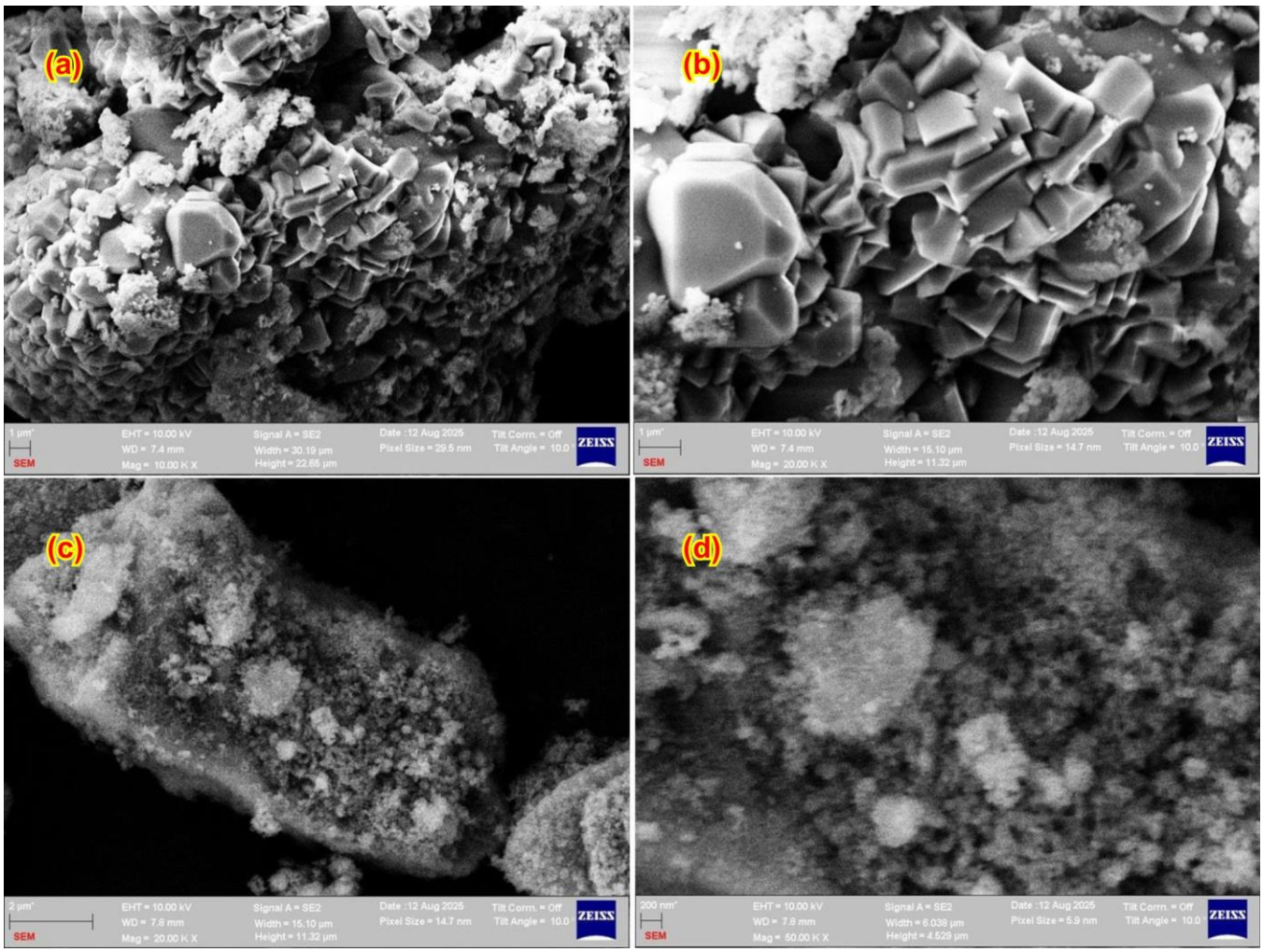

Fig. 2. FESEM images of Fe_2O_3 nanoparticles prepared by co-precipitation (a & b) and green synthesis (c & d) methods

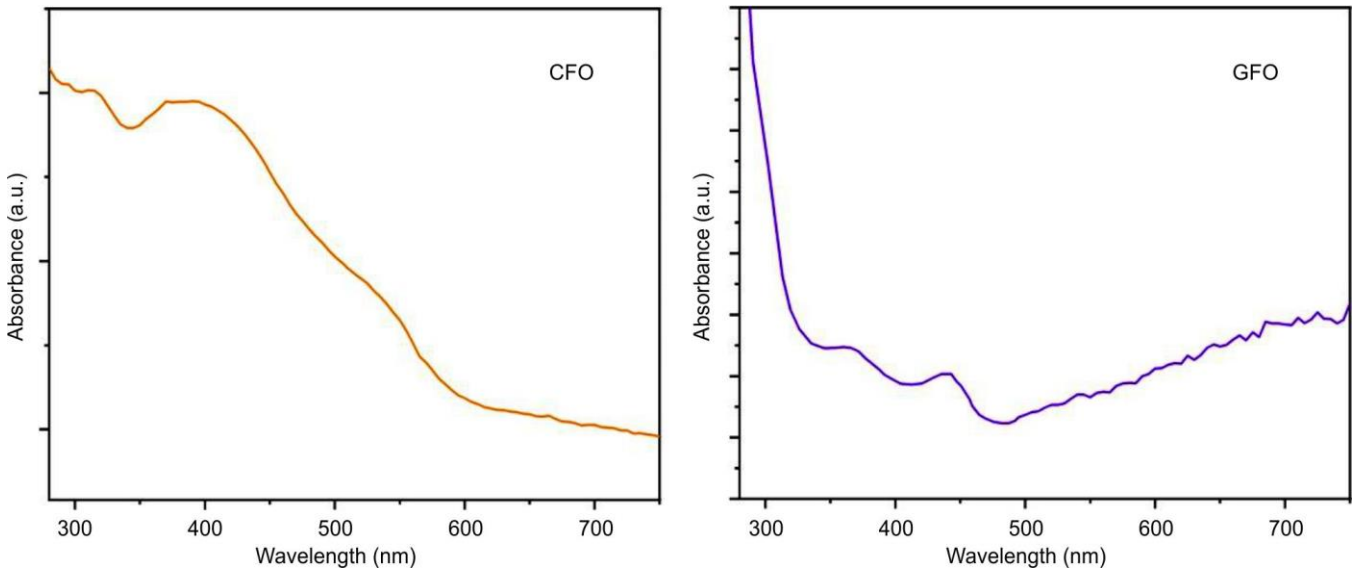

Fig. 3. UV-Vis absorbance spectra of Fe_2O_3 nanoparticles

the Neem extract utilized during the green technique [31,32]. Bandgap energies (E_g) were estimated using the Tauc's plot (Fig. 4) method based on the relation $(\alpha h\nu)^n = A(h\nu - E_g)$ with n = 2 for direct allowed transitions. The calculated band-gap values are approximately 2.33 eV for GFO and 2.43 eV for CFO, consistent with reported values for α-Fe_2O_3 nano-

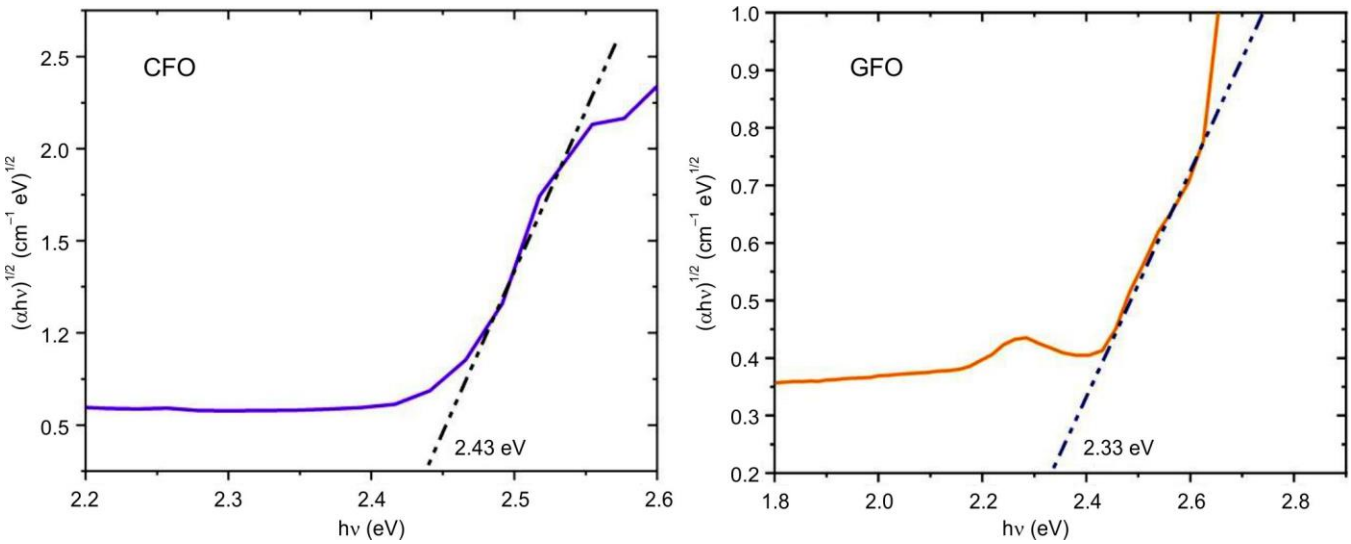

Fig. 4. Tauc's plot for Fe_2O_3 nanoparticles

structures [30-32]. The narrower bandgap of the GFO sample can be ascribed to the formation of surface states introduced by organic components from the green synthesis route, which promote sub-bandgap absorption.

FTIR studies: The FTIR spectra of Fe_2O_3 nanoparticles are shown in Fig. 5. The Fe–O bond-specific vibrational modes appearing in each spectrum clearly indicate that iron oxide nanoparticles have been effectively produced. The strong absorption bands in the range 580-560 cm^{-1} are assigned to Fe–O stretching vibrations in the α-Fe_2O_3 lattice, validating the formation of the hematite phase in both samples [33]. For the GFO sample, additional peaks are observed around 3400 cm^{-1} and 1630 cm^{-1}, hydroxyl groups and water molecules adsorbed on the surface are responsible for the O–H vibrational modes represented by these bands [34]. These enhanced bands in GFO compared to CFO indicate the presence of bioactive phytochemicals from neem leaf extract, which act as capping and stabilizing agents during green synthesis. Weak bands between 2920-2850 cm^{-1} can be assigned to stretching vibrations of C–H compounds, further supporting the role of plant-derived biomolecules [34]. In the CFO spectrum, the absence or weakening of these organic-related peaks signifies a relatively cleaner surface without bioorganic residues. The sharper and slightly more intense Fe–O bands in CFO indicate better crystallinity.

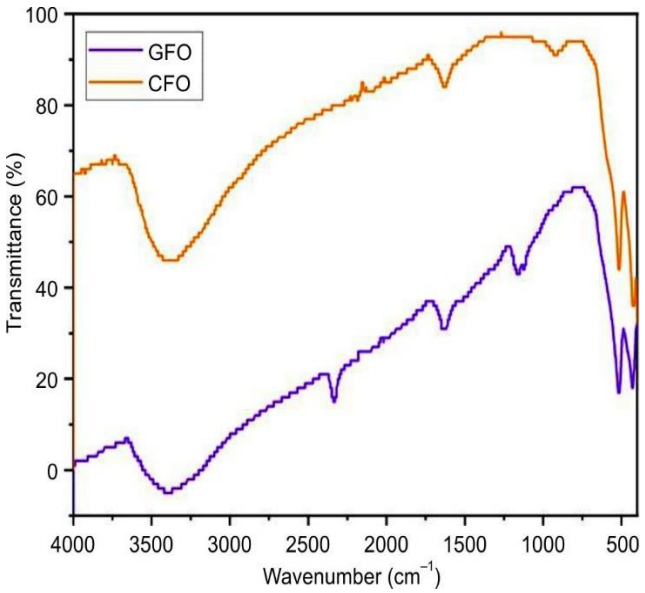

Fig. 5. FTIR spectra of Fe_2O_3 nanoparticles

Antibacterial activity: Evaluation of Fe_2O_3 nanoparticles through the agar well-diffusion assay highlighted notable differences in antibacterial activity between green and chemically synthesized variants of Fe_2O_3. The green-synthesized particles (GFO) achieved inhibition zones of around 20 ± 0.5 mm against *E. coli* and 17 ± 0.4 mm against *S. aureus*, signifying superior activity. In contrast, the chemically synthesized counterparts (CFO) displayed reduced effectiveness, producing zones of only 15 ± 0.3 mm for *E. coli* and 13 ± 0.2 mm for *S. aureus*. These values are summarized in Table-1. This observed enhancement in antibacterial efficacy of GFO sample can be attributed to its smaller crystallite size, higher surface area and the presence of phytochemical functional groups from neem extract [16,24]. These biomolecules facilitate better dispersion and improved interaction of the nanoparticles with the bacterial cell membrane, enabling deeper penetration and more effective bacterial inhibition [16]. Differences in antibacterial response between *E. coli* and *S. aureus* are closely linked to their cell wall composition. The cell envelope of *E. coli* is characterized by a porous lipid outer membrane and a thinner peptidoglycan structure, allowing easier nanoparticle inter-

TABLE-1
VALUES OF ZONE OF INHIBITION FOR Fe_2O_3 SAMPLES

Sample	ZOI (mm)	
	E. coli	*S. aureus*
CFO	12.3±0.02	23.6±0.03
Negative control (gentamicin-50 µg/mL)	07.3±0.01	13.4±0.02
Positive control (saline water)	11.3±0.02	24.3±0.03
GFO	14.7±0.05	20.6±0.03
Negative control (gentamicin-50 µg/mL)	08.3±0.03	11.4±0.01
Positive control (saline water)	10.3±0.01	23.3±0.02

action. Conversely, the robust, thick peptidoglycan layer of *S. aureus* reduces permeability, thereby conferring partial resistance to nanoparticle activity.

Mechanism: Fig. 6 demonstrates that the antimicrobial mechanism of Fe_2O_3 nanoparticles is predominantly linked to oxidative stress induced by reactive oxygen species (ROS). Among these, hydroxyl radicals ($^{\bullet}OH$), superoxide anions ($O_2^{\bullet-}$) and hydrogen peroxide (H_2O_2) act synergistically to compromise bacterial cell integrity [16,19,20,35]. These ROS attack bacterial membranes, proteins and nucleic acids, leading to lipid peroxidation, protein denaturation, enzyme inactivation and DNA damage, ultimately resulting in the cell death [16, 19,20,24]. In addition to ROS generation, the nanoparticles interact directly with bacterial cell surfaces, leading to membrane disruption, cytoplasmic leakage and subsequent impairment of essential metabolic processes [24,35].

The superior performance of GFO nanoparticles is linked to a synergistic effect where phytochemicals from the neem extract not only cap and stabilize the nanoparticles but also enhance ROS generation and facilitate stronger electron transfer, intensifying oxidative stress in bacterial cells [16,24,35,36]. This dual antibacterial mechanism *i.e.* physical damage to cell envelopes combined with oxidative stress accounts for the larger inhibition zones observed with GFO, emphasizing its potential as an eco-friendly and highly effective antibacterial agent [35,36]. These findings highlight the role of green synthesized Fe_2O_3 nanoparticles for applications in biomedical devices, antibacterial coatings and wastewater disinfection, where enhanced efficacy and environmental compatibility are essential.

Conclusion

Fe_2O_3 nanoparticles were synthesized in this study using two different methodologies; one based on the conventional co-precipitation process and the other on a green biosynthetic route utilizing *A. indica* (neem) leaf extract. Structural, morphological, optical and antibacterial investigations revealed that both synthesis techniques yielded crystalline α-Fe_2O_3 nanoparticles; however, the green synthesis route offered distinct advantages. The XRD results demonstrated that the Fe_2O_3 nanoparticles were phase-pure and crystalline, while also revealing that crystallite sizes were reduced in the green-synthesized samples compared to their conventionally prepared counterparts. FESEM images also showed a more uniform morphology and better dispersion for green synthesized Fe_2O_3. UV-Vis studies indicated strong absorption in the visible region and the band gap analysis confirmed slight tunability in the green-synthesized nanoparticles, reflecting the influence of biomolecules from the neem extract. FTIR spectra validated the presence of Fe–O bonds along with functional groups from the plant extract, indicating effective capping and stabilization of the nanoparticles. The results of antibacterial testing indicated that green-synthesized Fe_2O_3 nanoparticles (GFO) possessed significantly enhanced antimicrobial efficacy toward *E. coli* and *S. aureus* in comparison with co-precipitated Fe_2O_3 nanoparticles. The enhanced performance of GFO is attributed to its smaller size, higher surface area and the presence of phytochemicals facilitating greater interaction with bacterial cells and a surge in ROS generation, leading to membrane disruption and cell death. Overall, this study highlights the potential of green-synthesized Fe_2O_3 nanoparticles as eco-friendly, effi-

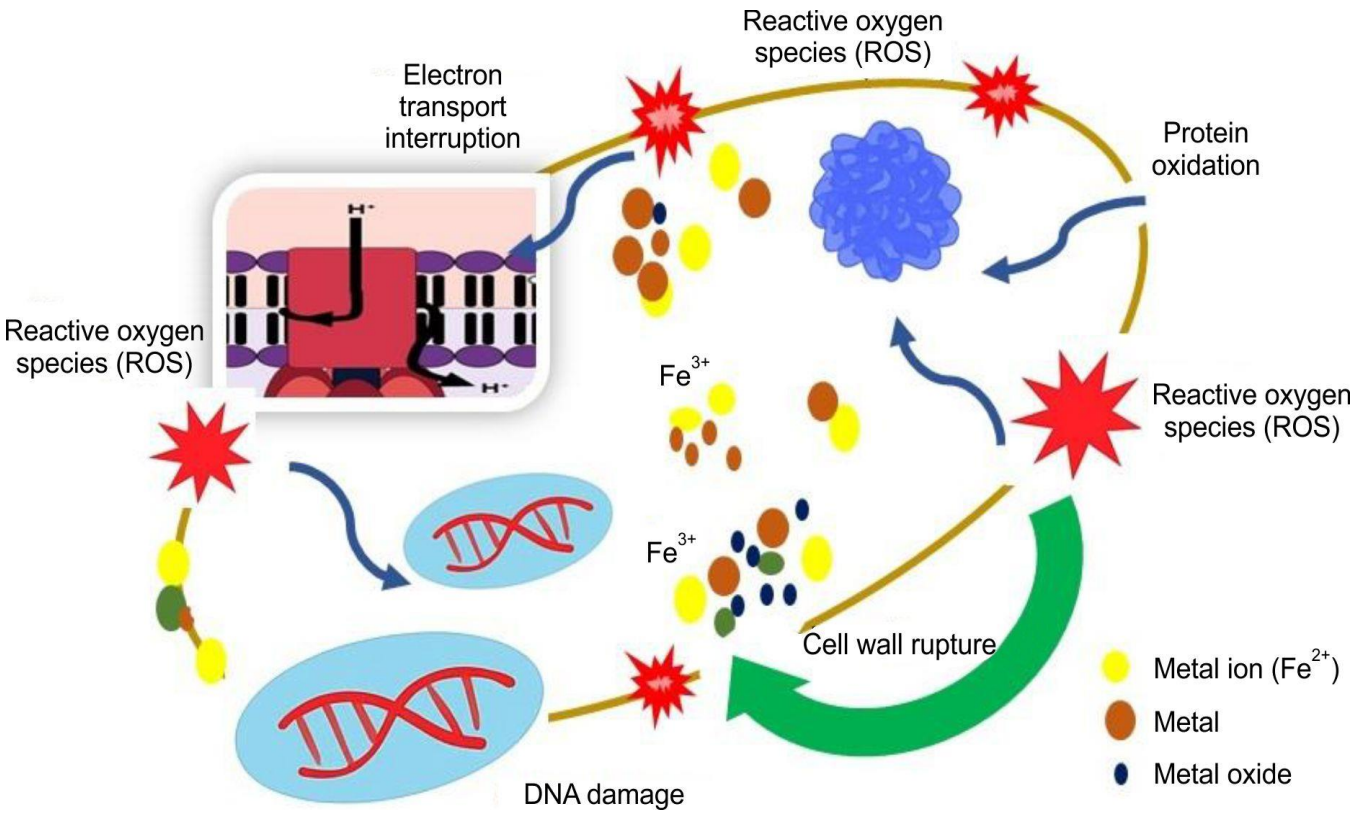

Fig. 6. Antibacterial mechanism in Fe_2O_3 nanoparticles

cient antibacterial agents for biomedical, environmental and industrial applications, combining superior functional properties with sustainable synthesis routes.

CONFLICT OF INTEREST

The authors declare that there is no conflict of interests regarding the publication of this article.

DECLARATION OF AI-ASSISTED TECHNOLOGIES

During the preparation of this manuscript, the authors used an AI-assisted tool(s) to improve the language. The authors reviewed and edited the content and take full responsibility for the published work.

REFERENCES

1. Z. Lei, J.M. Lee, G. Singh, C.I. Sathish, X. Chu, A.H. Al-Muhtaseb, A. Vinu and J. Yi, *Energy Storage Mater.*, **36**, 514 (2021); https://doi.org/10.1016/j.ensm.2021.01.004
2. S.O. Ogungbesan, N.O. Etafo, O.H. Anselm, O. Ejeromedoghene, M. Kalulu, M. Abdullah, D.D. Diaz and G. Fu, *J. Mol. Struct.*, **1337**, 142209 (2025); https://doi.org/10.1016/j.molstruc.2025.142209
3. A. D'Souza, R.S. Kurale, D. Kumar, P. Rakesh and R. Kumar, *Bionanoscience*, **15**, 408 (2025); https://doi.org/10.1007/s12668-025-02020-3
4. J.-M. Kim, X. Zhang, J.-G. Zhang, A. Manthiram, Y.S. Meng and W. Xu, *Mater. Today*, **46**, 155 (2021); https://doi.org/10.1016/j.mattod.2020.12.017
5. I.S. Okeke, E.O. Echeweozo, A.C. Ogu, P.Y. Aondona and F.I. Ezema, *Hybrid Adv.*, **7**, 100322 (2024); https://doi.org/10.1016/j.hybadv.2024.100322
6. D.S. Chaudhari, R.P. Upadhyay, G.Y. Shinde, M.B. Gawande, J. Filip, R.S. Varma and R. Zbořil, *Green Chem.*, **26**, 7579 (2024); https://doi.org/10.1039/D4GC01870B
7. D. Kumar Chelike, P. Mehta and A. Kumar, *Inorg. Chem. Commun.*, **166**, 112611 (2024); https://doi.org/10.1016/j.inoche.2024.112611
8. M. Mishra and D.-M. Chun, *Appl. Catal. A Gen.*, **498**, 126 (2015); https://doi.org/10.1016/j.apcata.2015.03.023
9. M. Białek, J. Zhang, H. Yu and J.-Ph. Ansermet, *Appl. Phys. Lett.*, **121**, 032401 (2022); https://doi.org/10.1063/5.0094868
10. N.R. Panda, B.S. Acharya, P. Nayak, S.P. Pati, B.K. Nath and D. Das, *Physica B*, **407**, 2716 (2012); https://doi.org/10.1016/j.physb.2012.03.071
11. N.R. Panda, D. Sahu, B.S. Acharya, P. Nayak, S.P. Pati and D. Das, *Acta Metall. Sin.*, **27**, 563 (2014); https://doi.org/10.1007/s40195-014-0093-8.
12. E.M. Materón, C.M. Miyazaki, O. Carr, N. Joshi, P.H.S. Picciani, C.J. Dalmaschio, F. Davis and F.M. Shimizu, *Appl. Surf. Sci. Adv.*, **6**, 100163 (2021); https://doi.org/10.1016/j.apsadv.2021.100163
13. L.V. Hublikar, S.V. Ganachari, F.A. Shilar and N. Raghavendra, *Mater. Res. Bull.*, **187**, 113351 (2025); https://doi.org/10.1016/j.materresbull.2025.113351
14. S. Haseena, S. Shanavas, T. Ahamad, S.M. Alshehri, J. Duraimurugan, P. Baskaran, R. Acevedo, M.A.M. Khan, P.M. Anbarasan and N. Jayamani, *J. Environ. Chem. Eng.*, **9**, 104996 (2021); https://doi.org/10.1016/j.jece.2020.104996
15. H.J. Mayouf, M.F. Naief, S.N. Mohammed and A.M. Mohammed, *J. Organomet. Chem.*, **1029**, 123543 (2025); https://doi.org/10.1016/j.jorganchem.2025.123543
16. H.J. Fatih, M. Ashengroph, A. Sharifi and M.M. Zorab, *BMC Microbiol.*, **24**, 535 (2024); https://doi.org/10.1186/s12866-024-03699-2
17. F. Dehdashti, H. Shirkani, M. Mehrabi and A. Ahmadi, *Sci. Rep.*, **15**, 32269 (2025); https://doi.org/10.1038/s41598-025-17797-2
18. R. Vinayagam, S. Pai, T. Varadavenkatesan, M.K. Narasimhan, S. Narayanasamy and R. Selvaraj, *Surf. Interfaces*, **20**, 100618 (2020); https://doi.org/10.1016/j.surfin.2020.100618
19. M.A. Rabbi, M. Bithi Akter, B.M. Chaki, M. Abdul Latif, M. Al-Amin, M. Zia Uddin Rasel, S. Sharmin, M. Abdurrahim, M.H.K. Rubel and M.R. Habib, *New J. Chem.*, **48**, 5278 (2024); https://doi.org/10.1039/D3NJ05885A
20. F. Naushin, S. Sen, M. Kumar, H. Bairagi, S. Maiti, J. Bhattacharya and S. Sen, *ACS Omega*, **9**, 464 (2024); https://doi.org/10.1021/acsomega.3c05930
21. A.V. Samrot, C.S. Sahithya, J. Selvarani A, S.K. Purayil and P. Ponnaiah, *Curr. Res. Green Sustain. Chem.*, **4**, 100042 (2021); https://doi.org/10.1016/j.crgsc.2020.100042
22. S. Kumar, M. Kumar and A. Singh, *Contemp. Phys.*, **62**, 144 (2021); https://doi.org/10.1080/00107514.2022.2080910
23. A. Lassoued, B. Dkhil, A. Gadri and S. Ammar, *Results Phys.*, **7**, 3007 (2017); https://doi.org/10.1016/j.rinp.2017.07.066
24. O. Elkhateeb, M.B. Atta and E. Mahmoud, *AMB Express*, **14**, 92 (2024); https://doi.org/10.1186/s13568-024-01746-9
25. M.A. Shabbir, M. Naveed, S.U. Rehman, N.U. Ain, T. Aziz, M. Alharbi, A. Alsahammari, A.F. Alasmari and A.F. Alasmari, *ACS Omega*, **8**, 33358 (2023); https://doi.org/10.1021/acsomega.3c02744
26. A. Mohamed, R.R. Atta, A.A. Kotp, F.I. Abo El-Ela, H. Abd El-Raheem, A. Farghali, D.H.M. Alkhalifah, W.N. Hozzein and R. Mahmoud, *Sci. Rep.*, **13**, 7227 (2023); https://doi.org/10.1038/s41598-023-31704-7
27. S. Salim, N. Hari, S. Sudhi and A.J. Nair, *Microbe*, **8**, 100481 (2025); https://doi.org/10.1016/j.microb.2025.100481
28. S.P. Patil, R.Y. Chaudhari and M.S. Nemade, *Talanta Open*, **5**, 100083 (2022); https://doi.org/10.1016/j.talo.2022.100083
29. N.D.S. Zambri, N.I. Taib, F. Abdul Latif and Z. Mohamed, *Molecules*, **24**, 3803 (2019); https://doi.org/10.3390/molecules24203803
30. S.E. Chamberlin, Y. Wang, K. Lopata, T.C. Kaspar, A.W. Cohn, D.R. Gamelin, N. Govind, P.V. Sushko and S.A. Chambers, *J. Phys. Condens. Matter*, **25**, 392002 (2013); https://doi.org/10.1088/0953-8984/25/39/392002
31. D. Tahir, S. Ilyas, R. Rahmat, H. Heryanto, A.N. Fahri, M.H. Rahmi, B. Abdullah, C.C. Hong and H.J. Kang, *ACS Omega*, **6**, 28334 (2021); https://doi.org/10.1021/acsomega.1c04526
32. S. Piccinin, *Phys. Chem. Chem. Phys.*, **21**, 2957 (2019); https://doi.org/10.1039/C8CP07132B
33. K. Supattarasakda, K. Petcharoen, T. Permpool, A. Sirivat and W. Lerdwijitjarud, *Powder Technol.*, **249**, 353 (2013); https://doi.org/10.1016/j.powtec.2013.08.042
34. F. Gheybi, M. Rashidi-Huyeh and M.R. Mohammadi, *Discov. Mater.*, **5**, 132 (2025); https://doi.org/10.1007/s43939-025-00310-x
35. P.N.V.K. Pallela, S. Ummey, L.K. Ruddaraju, S. Gadi, C.S.L. Cherukuri, S. Barla and S.V.N. Pammi, *Heliyon*, **5**, e02765 (2019); https://doi.org/10.1016/j.heliyon.2019.e02765
36. L. Sihem, D. Hanine and B. Faiza, *Nanotechnol. Russ.*, **15**, 198 (2020); https://doi.org/10.1134/S1995078020020135